

Hierarchical self-assembly of suspended branched colloidal nanocrystals into superlattice structures

K. Miszta, J. de Graaf, G. Bertoni, D. Dorfs, R. Brescia, S. Marras, L. Ceseracciu, R. Cingolani, R. van Roij, M. Dijkstra and L. Manna

Table of Contents

1. Synthesis of Octapods
2. Supplementary Discussions
3. Supplementary Figures and Tables
4. Supplementary Notes

1. Synthesis of Octapods

In a typical synthesis, 6 g of trioctylphosphine oxide, 160 mg of hexylphosphonic acid, 580 mg of octadecylphosphonic acid and 120 mg of cadmium oxide (CdO) were placed in a three-neck flask connected to a Schlenk line. The flask was pumped to vacuum while the mixture was heated to 150 °C for 120 min under vigorous stirring, after which the solution was put under a blanket of nitrogen and the temperature was raised to 350 °C. At this point 1.6 g of trioctylphosphine were injected with a syringe, and the mixture was allowed to recover to 350 °C. Previously prepared and purified Cu_{2-x}Se nanocrystals were dissolved in trioctylphosphine (TOP) inside the glove box. A stock solution for the injection was prepared by dissolving 16 mg of elemental sulphur in 0.5 mg of TOP, and then by adding the previously prepared and purified Cu_{2-x}Se nanocrystals in a concentration of 0.3 ·10⁻⁹ mol. This solution was quickly injected in the reaction flask via a syringe, and the resulting mixture was allowed to recover at the pre-injection temperature (i.e., 350 °C). Ten minutes after the injection, the heating mantle was removed and the flask was allowed to cool to room temperature. The solution was then washed by repeated precipitations (via addition of methanol) and redissolutions in toluene. After the last washing step, the octapods were dissolved in 5 ml of toluene or chloroform.

2. Supplementary Discussions

Comparison between chloroform and toluene solutions. Figure S1 shows dynamic light scattering (DLS) cluster size distribution curves and corresponding low temperature scanning transmission electron microscopy (cryo-STEM) images from octapods in chloroform solution (Figs. S1a-c), and from octapods in toluene solution (Figs. S1d-f). It is evident from the

experiments that in chloroform chain structures are not seen initially, nor after 24 h ageing. In toluene clear evidence of chain formation comes both from DLS curves (showing an increase in particle size with time from $0.18 \pm 0.12 \mu\text{m}$ at initial ageing to $0.34 \pm 0.17 \mu\text{m}$ after 24 h ageing) and from the STEM images from a solution aged for about 24 h, and vitrified on a C-flat grid by plunge freezing (the round regions correspond to the C-flat grid film holes filled with solution). From the STEM images, an average chain length of $0.38 \pm 0.15 \mu\text{m}$ was measured, corresponding to an average of $N = 11 \pm 4$ octapods per chain, in agreement with DLS (all uncertainties numbers are given as standard deviations from the mean values).

Comparison between structures obtained in toluene and toluene/acetonitrile solutions.

In Fig. S2 we present scanning electron microscopy (SEM) images comparing the structures obtained in the toluene solution with the ones obtained after mixing with acetonitrile (with toluene/acetonitrile volume ratio equal to 20/80), without performing any size selection from the solutions. In toluene, in agreement with cryo-STEM measurements (Figs. S1d-f), chains are visible, with average length $0.41 \pm 0.09 \mu\text{m}$, or approximately $N = 12 \pm 3$ octapods per chain (with an average octapod-octapod distance in the chains equal to $37 \pm 2 \text{ nm}$). In acetonitrile three dimensional (3D) clusters are clearly formed, with average length along the chain axis $L = 2.00 \pm 0.26 \mu\text{m}$, and average width/height $W = H = 0.99 \pm 0.22 \mu\text{m}$. A wetting layer of chains is also left on the substrate by evaporation of the solvent. It is evident that chains are longer in the case of toluene/acetonitrile mixture, with average length $0.90 \pm 0.29 \mu\text{m}$, or approximately $N = 27 \pm 8$ octapods per chain (with an average octapod-octapod distance in the chains equal to $35 \pm 2 \text{ nm}$). Note that the average chain length can be underestimated in the latter case, most likely because the longest chains have already assembled into 3D superstructures.

1D and 3D superstructures models. For better clarity the observed 1D chain structure and 3D assembly are sketched in Fig. S3. The chain consists of octapods interlocked with each other in two orientations (magenta and blue octahedrons in Fig. S3a), the second one rotated by 45° around a $<100>$ direction of the cube spanned by the tips of the octapod. The 3D structure is formed by packing the chains in two orthogonal directions, both perpendicular to the chain axis, in the same way for each direction, i.e., by making the pods of octapods facing each other. This results in a tetragonal unit cell consisting of two interpenetrating lattices (one formed by the magenta octahedrons and one formed by the blue ones). The c-axis of the tetragonal cell is parallel to the chain axis (or the $<100>$ direction of the cube spanned by the tips of the octapod), and rotated by 45° with respect to the substrate surface normal. The clusters have some defects in the structures, due to missing chains, missing octapods in the chains, and slight tilts of chains or octapods in a chain. In Fig. S4 we show a region with two missing chains in the structure, revealing the underneath layer with the expected structure of Fig. S3, together with some missing octapods (black octapods in the enlarged sketch in the right), resulting in a slight distortion.

EDS chemical mapping and quantification. We monitored the cation exchange (CE) and O₂ plasma (CEP) effects by energy dispersive X-ray spectroscopy (EDS), which was performed on the same sample at both process steps. The results are shown in Fig. S5. For every step we report a close-up view of chain arrangement in the 3D structure, together with an overview of a cluster of 3D superstructures and chemical maps of the representative elements. The extent of exchange (i.e., amount of Cd exchanged), calculated from the ratio between the Cd L α peak area after and before the cation exchange process, is $87 \pm 2\%$ after 15 min of exchange, and $92 \pm 2\%$ after 2 h of exchange. The linking of the chains after CEP is evident from the close-up view of Fig. S5c. Moreover, the clusters stay intact during the processes, as revealed by the low magnification images. To verify the formation of a Cu oxide shell surrounding the pods, we performed a ‘ZAF’ quantification³⁴ of the O/Cu ratio averaged over the clusters in Fig. S5. We took care to consider only molar variation of oxygen after plasma treatment with respect to the same sample before plasma treatment. In addition, we subtracted the contribution of oxygen coming from the substrate (silicon with its native oxide, wetting organic residuals, etc.), by taking a spectrum from a region with no clusters. The results were compared with a simple model for each pod consisting of a cylinder of Cu₂S (diameter $d = 12$ nm) surrounded by a 3 nm Cu₂O shell (note that an equilateral triangular section for the pod with edge length d gives the same result). The quantification of the O/Cu ratio gave 0.21 ± 0.02 , not far from the calculated value from the simple model (0.28) pointing to shell oxidation also for inner chains of the clusters (an oxidation of only external pods likely gives a much lower value).

EFTEM chemical maps and TEM investigations after cation exchange and O₂ plasma treatment (CEP). To verify the external shell consists of copper oxide after CEP, we acquired energy filtered transmission electron microscopy (EFTEM) chemical maps of Cu (L edge at 931 eV), O (K edge at 532 eV), S (L edge at 165 eV), and C (K edge at 284 eV) after deposition on a holey carbon support grid, and following a chemical treatment very similar to the one in the previous section. In particular, we wanted to make sure that the oxygen found by EFTEM was not deriving predominantly from a residual organic capping layer surrounding the pods, rather than from an inorganic oxide shell. In the case of an organic shell we should expect a corresponding intense carbon signal from the shell. In Fig. S6 the elemental maps of the four elements are shown for a chain portion. Clearly, the carbon signal from the shell is extremely low. The main carbon signal comes from the few nm thick carbon support film of the grid (bottom left region in the C map), and from a few interstitial regions with organic residuals, or background signal from thick regions (i.e., when the pods overlaps). Transmission electron microscopy (TEM) investigations on the same sample after plasma treatment (CEP) reveal (Fig. S7) a mainly amorphous (oxide) shell (approximately 3 nm thick) surrounding the octapods, in agreement with Cu and O maps from EFTEM of Fig. S6. Organic residuals in interstitial regions are sometimes found, giving a low contrast similar to that of amorphous carbon.

Nanoindentation fracture toughness evaluation. As a preliminary mechanical characterization, fracture was induced to 3D structures after either only the cation exchange

treatment (CE), or both the cation exchange and O₂ plasma treatments (CEP), respectively. A large number of indentations (100) were performed in areas with high concentration of clusters. The difference in the load-depth curves obtained on clusters, compared with the ones that had indented only silicon, shown in Fig. S8, is evident. In the former case, the indenter tip has to cut through the structure before reaching the silicon substrate. The load reached in the process, indicated by the arrow in the inset of Fig. S8, is an indirect measurement of the fracture energy of the cluster. The values extracted were 98 ± 26 μN and 124 ± 40 μN for CE and CEP samples, respectively. Despite the high standard deviation due to the stochastic approach, we consider that the number of valid indentations (25 on the CE sample, 35 on the CEP sample) is large enough to provide reliable indications of the toughness improvement.

Monte Carlo simulations of hard octapods. We performed isothermal-isobaric (*NPT*) Floppy Box Monte Carlo³⁵ (FBMC) simulations, regular *NPT* Monte Carlo (MC) simulations and isothermal-isochoric (*NVT*) MC simulations to verify that the experimentally observed structures cannot be formed by excluded-volume interactions only and as a means to test the speed and efficiency of the simulations. Such relatively basic hard-particle interactions are, however, already very complicated due to the unusual shape of the octapod nanocrystals. Therefore, we used triangular tessellation³⁶ in order to determine overlaps between two octapods. The overlap checks can be handled on the level of simple triangular base constituents³⁷ by finding a suitable tessellation, instead of setting up a complex octapod-octapod overlap routine. The FBMC technique is a numerical scheme to predict crystal structures. It greatly reduces the difficulty of studying crystal structures by considering them on the level of the unit cell. We have based the model for the octapods used in simulations on the experimental STEM tomography results (Figs. 1a,d). The following quantities are used here to uniquely define the shape of the octapod model, also see Fig. S9a, which shows this model and indicates various length scales. The edge length of the octahedral CdSe core is given by $l_c = 22$ nm, the edge length of the triangular tip of the octapod by $l_t = 15$ nm, and the length of the pod by $l_a = 62$ nm, which is measured from the centre of the octapod to the centroid of the triangular tip. We note that this model does not include the small added width caused by the presence of a capping layer, which one could consider a soft-potential effect. We determined crystal structure candidates for the octapods by the FBMC method. We repeatedly compressed a system of octapods from a dilute-gas phase to a high-density state for several values of $N = 1, \dots, 6$, with N the number of particles in the unit cell. Thereby, we found several high-density crystal structures, none of which (over 1000 trials with varying compression rates), however, corresponded to the experimentally observed crystal (see Fig. 2). We therefore concluded that the hard-particle model, for which the system is governed by excluded volume interactions, is not able to correctly describe the experimentally observed assembly of octapods into 3D superstructures. This was actually expected on the basis of the experimental results, since the initial chain-formation step before crystallisation and the dilution at which this occurs, is indicative of a system which is driven by attractive interactions. The lack of superstructure and chain formation of the hard-particle model was further confirmed by performing standard *NVT* MC simulations at high volume fractions $\phi \approx 0.2$, as well as regular *NPT* MC simulations at pressures for which the system ‘crystallises’. In these simulations only irregular clusters of octapods were found. Similarly, during gas

phase *NPT* and *NVT* simulation studies, we did not observe any chain-like structures to form spontaneously.

Interlocked chains for octapods with empirical attractive interactions. For the next phase of our investigation, we focused on reproducing the experimentally observed chain formation in toluene at low volume fractions, which is an important step in the superstructure formation process. We studied a variety of simple soft potentials, in addition to the hard-particle interactions, in order to empirically determine a combination that produces the experimental structures. Here we were limited by the computational difficulties to very basic potential types and small system sizes. We found that the formation of chains in the dilute phase is accomplished by a model where not only the octahedral cores attract each other, but where the tips of the octapods also attract each other. The model we settled upon employs a Lennard-Jones (LJ) interaction $U_{\text{LJ}}(r)$ between the cores and a square-well (SW) interaction $U_{\text{SW}}(r)$ between the centroids of the tips. Figure S9a shows a representation of the LJ and SW interaction potentials. In the configuration of Fig. S9a the LJ interaction is given by

$$U_{\text{LJ}}(r) = \varepsilon_l \left\{ \left(\frac{r_m}{r} \right)^{12} - 2 \left(\frac{r_m}{r} \right)^6 \right\}, \quad (1)$$

with r the centre-to-centre distance between two octapods, $r_m \approx l_a/\sqrt{3}$ the location of the minimum, and $\varepsilon_l \approx 8 kT$ the well depth, where k is Boltzmann's constant and T is the temperature. The value of r_m has been chosen such that, in an interlocking chain configuration, each octapod is located in the 'double-well' of the 'cage' formed by its two adjacent octapods (provided it is not on the end of the chain). Figure S9b shows this effect. To fixate the chains such that the tips of the octapods touch in the interlocking configuration a spherical square well was implemented

$$U_{\text{SW}}(r) = \begin{cases} -\varepsilon_s & : r < \sigma \\ 0 & : r > \sigma \end{cases}, \quad (2)$$

with r the centroid-to-centroid distance between the triangular tips of the octapod pods, $\sigma \approx l_a/2$ the range of the interaction, and $\varepsilon_s \approx 4 kT$ the well depth. Small changes in the model did not interfere with the formation of chains, although the ease of formation and the stability of the chains vary significantly over a range of $1 kT$ in the depth of either interaction potential. The choice for the LJ interaction was inspired by the idea that van der Waals (vdW) interactions are probably the dominant factor in the self-assembly of octapods and this potential can be used to approximate a vdW interaction combined with steric repulsive effects. A medium ranged SW interaction between the cores of the octapods was also considered initially, but it did not produce chains of the same length and quality as the LJ core-core interaction. We have also studied the addition of attractive Yukawa-like tails to make the range of the SW potential slightly longer. However, we found the short-ranged SW-like part of the interaction to be essential in properly fixating the chains for this particular

model. The large well-depth used in both the LJ and SW potentials is required to achieve spontaneous formation of relatively stable chains at low densities $\phi \approx 0.01$, see Fig. 1b.

Using this empiric model in *NVT* MC simulations we observed the formation of chains containing as many as 5 octapods in the interlocking configuration for fairly dilute systems $\phi \approx 0.01$. Figure S9c shows a snapshot of an *NVT* simulation box containing 16 particles, most of which have formed interlocking-chain segments. All particles in the dilute systems that we have considered eventually became part of a chain through on-end attachment. For higher density, both branching and non-chain trimer formation were observed as well. Aggregation of the chains into structures with greater hierarchy, such as sheets or crystal structures was, however, not observed. Theoretical calculations on this model show that chain lengths exceeding 20 octapods are required to make on-end lengthening of the chain energetically less favourable than by side-by-side assembly of two chains. Figure S9d shows the interaction energy for on-end lengthening and the side-by-side interaction energy as a function of the number of octapods M in each of the two chains. The side-by-side aggregation of chains does not yield the experimentally observed morphology, where the pods of different chains interlock. Instead, we find a configuration where the chains touch at the tips, see the representation in Fig. S9d. This was further confirmed by *NVT* MC (and limited FBMC) simulations of rigid pre-assembled chains, which did not allow detachment of octapods from the chain. These simulations also showed tip-tip touching for the side-by-side chains with this model.

For dilute systems, $\phi \approx 0.01$, cluster moves could have been employed to accelerate the exploration of phase space. We did not pursue this method here for the following reason. Cluster moves would speed up the initial on-end lengthening and sideways aggregation of the chains, but, when these chains come in close proximity of one another, the majority of the accepted moves would be either single particle translations or rotations. For these single particle moves we are limited by the computational efficiency of our method, namely the prohibitive number of individual octapods required to simulate several long chains in one box. The stiff pre-assembled chains thus form a compromise between computational efficiency and the area of phase space that can be sampled. Moreover, at higher packing fractions, $\phi \approx 0.1$, the highly non-convex nature of the octapods makes it difficult to identify clusters and to move such clusters, since the octapods can form a kind of ‘briar patch’ through which single particles cannot easily pass, let alone clusters. On the basis of our simulation results, we cannot exclude that these dense systems were kinetically arrested, but it is unlikely that the use of cluster moves would have been able to overcome any such arrest.

In the FBMC simulations using this empiric model we observed a variety of crystal structures, which did not possess the chain-like morphology. For the most part, configurations where the tips of the pods are in close proximity were found, which differ from the experimentally observed 3D superstructure because they either did not interlock or, if they did, they did not possess the ‘pod-pod’ parallel configuration. On occasion, however, we did find structures similar to those observed in the experiments, possessing both the interlocked and the ‘pod-pod’ parallel configuration. We attribute these occurrences to an increased probability of interlocking aggregation taking place, when compressing further from the fluid phase, due to the core-core attractions. This led us to conclude that the LJ-SW model only partially captures the physics of the experimental system, namely the formation of chains in the dilute fluid phase. Upon examining the evidence that interactions between the cores of the

octapods play an important role in chain formation, we decided to perform theoretical calculations to see to what extent these can be explained by vdW interactions. We did not proceed with such calculations beforehand, because of the numerical challenges such calculations bring about.

Hamaker-de-Boer calculation of the van-der-Waals interaction between two octapods. Calculating the vdW interactions between two octapods is extremely complicated, due to the geometry of the particle and the high dimensionality of the parameter space which can be explored. Our analysis proceeds as follows. The non-retarded vdW interaction $U_{\text{vdW}}(r, \mathbf{u}, \mathbf{v})$ between two octapods, which are separated by a centre-to-centre distance r and have orientation unit vectors \mathbf{u} and \mathbf{v} respectively, can be computed using a Hamaker-de-Boer type integration³⁸ of inter-atomic dispersion forces, such that

$$U_{\text{vdW}}(r, \mathbf{u}, \mathbf{v}) = C\rho_1\rho_2 \int_{O_1} d\boldsymbol{\tau}_1 \int_{O_2} d\boldsymbol{\tau}_2 |\boldsymbol{\tau}_1 - \boldsymbol{\tau}_2|^{-6}, \quad (3)$$

where the volume integration takes place over the two octapods, for which the integration boundary of octapod $i = 1, 2$ is specified by O_i . The positions $\boldsymbol{\tau}_i$ are the integration variables, $|\cdot|$ is the Euclidean vector norm, C is the London constant associated with the octapod-medium-octapod dispersion interaction, and ρ_i is the number density of atoms in the i -th octapod. Note that the integration boundaries O_i are implicitly dependent on r , \mathbf{u} , and \mathbf{v} . Furthermore, the model assumes homogeneous density distributions ρ_i and a constant value of C . The London constant C is related to the Hamaker constant A for the octapod-medium-octapod interaction according to $A = 2\pi C\rho_1\rho_2$. Evaluating the integrals in Eq. (3) cannot be done analytically for the complex shape of the octapod. Therefore, we resort to a numerical scheme, where we have split the integration in Eq. (3) into two parts for the purpose of efficiency. Without loss of generality we can place one octapod in the origin, such that its pods are oriented along the $(\pm 1, \pm 1, \pm 1)$ vectors. For a point given by the vector \mathbf{r} , the vdW interaction ‘potential’ of this single octapod in the origin is given by

$$U_{\text{vdW,pnt}}(\mathbf{r}) = \frac{A}{\pi^2 \rho_2} \int_{O_1} d\boldsymbol{\tau}_1 |\boldsymbol{\tau}_1 - \mathbf{r}|^{-6}, \quad (4)$$

where O_1 is understood to be appropriately translated and rotated to place the octapod in the origin with the proper orientation. The vdW interaction between the two octapods is then given by

$$U_{\text{vdW}}(r, \mathbf{u}, \mathbf{v}) = \rho_2 \int_{O_2} d\boldsymbol{\tau}_2 U_{\text{vdW,pnt}}(\mathbf{r}), \quad (5)$$

where O_2 is subject to the same transformation operation as O_1 , thus preserving the configuration of interest. By tabulating the values obtained by evaluating Eq. (4) we can determine the vdW interaction for a given configuration using Eq. (5) in a computationally reasonable time.

In our analysis we exploit the symmetry of the octapod and tabulated Eq. (4) for one octant of the Cartesian coordinate system in a rectangular grid with 0.5 nm spacing up to 180 nm distance from the origin. Careful tailoring of the number of points in the numerical integration to ensure convergence to within 5% of the actual value of $U_{\text{vdW,pnt}}(\mathbf{r})$, allowed us to determine this landscape in roughly 4 days using 20 modern 2.0 GHz desktop PCs. The actual value of $U_{\text{vdW,pnt}}(\mathbf{r})$, which we used to determine an acceptable number of (equidistant) grid points (≈ 10 per nm) in the numerical integration, was calculated for several \mathbf{r} by using high precision integration. This high precision did however result in very slow numerical integration: roughly four hours per point. The point density used in the rectangular grid (0.5 nm spacing) is necessary to obtain a reasonable approximation to the vdW interaction between two octapods at close range when evaluating Eq. (5). Note that a cut-off at 180 nm from the origin in the tabulation of the potential landscape does not allow for a very large separation of the octapods, which themselves are 124 nm in diameter. We were limited in tabulating the vdW potential landscape to this range, due to time constraints and round-off errors, which become appreciable at large $|\mathbf{r}|$.

The \mathbf{r} dependence of $U_{\text{vdW}}(\mathbf{r}, \mathbf{u}, \mathbf{v})$, denoted by U_{vdW} for short, has been determined by evaluating Eq. (5) on the rectangular grid obtained in the previous step. We exploit the symmetry properties of the problem to mirror and rotate the pieces of octapod O_2 , which fall outside the tabulated octant, in such a way that they fall inside the octant after these operations. Since the tabulated potential of Eq. (4) is too large to store in random-access memory (RAM), roughly 5 GB of data, we implement a piecewise retrieval and integration strategy to evaluate Eq. (5). To improve the result, especially at close separation between the octapods, we implemented a trilinear interpolation scheme. Thereby, we managed to achieve a fractional uncertainty of around 0.15 for configurations where the octapods are within 3 to 6 nm of contact. We determined this uncertainty by fitting a higher order interpolation to the landscape and integrating that with high precision for several configurations, keeping in mind the 5% deviation already present in the landscape. Greater accuracies are achieved for greater separations. It takes around 30 minutes to evaluate Eq. (5) for a single configuration on a modern 2.0 GHz desktop computer with 2 GB of RAM.

Hamaker constants for the various octapod-medium-octapod interactions and incorporating steric repulsion. To determine the value of the vdW interaction for the experimental systems we require the Hamaker constant of the octapod-medium-octapod interaction for the three media used, namely chloroform, toluene, and acetonitrile. Here, we assume an equal Hamaker constant (over vacuum) for CdSe and CdS, $A_{\text{CdSe}} = A_{\text{CdS}} = 11.0 \cdot 10^{-20} \text{ J}$, in accordance with Refs. 39 and 40. The Hamaker constant of toluene over vacuum is given by $A_{\text{tol}} = 5.4 \cdot 10^{-20} \text{ J}$ according to Ref. 41. The Hamaker constant of CdSe/CdS over toluene is therefore $A_{\text{oto}} = (\sqrt{11.0} - \sqrt{5.4})^2 \cdot 10^{-20} \text{ J} = 9.9 \cdot 10^{-21} \text{ J}$, where we used the combining relations of Ref. 38. For chloroform we obtain $A_{\text{oco}} = 7.9 \cdot 10^{-21} \text{ J}$, because the Hamaker constant over vacuum for chloroform is $A_{\text{chl}} = 5.9 \cdot 10^{-20} \text{ J}$, according to Lifshitz theory³⁸ and the values in Ref. 42. Finally, for the toluene-acetonitrile mixture we obtain $A_{\text{oao}} = 1.5 \cdot 10^{-20} \text{ J}$, since $A_{\text{ace}} = 4.2 \cdot 10^{-20} \text{ J}$ over vacuum⁴³ and we have an 80% acetonitrile to 20% toluene solution (by volume), for which we can use the theory of Ref. 44. Note that the three Hamaker constants $A_{\text{oao}} > A_{\text{oto}} > A_{\text{oco}}$ differ significantly, which implies that the vdW forces

between the octapods in the various solutions also differ substantially, since the Hamaker constant acts as a multiplicative factor in U_{vdW} (see Eq. (4)).

To determine the short ranged repulsive interactions due to the presence of the octadecylphosphonic acid (ODPA) capping layer, we could have employed the Alexander-de-Gennes model³⁸. However, we abandoned this, because there are too many unknowns with respect to the properties of this capping layer in the experimental system. This is in part due the unknown affinity of the ODPA (i.e., the covering density) for the crystal facets of the octapod. In part, it is also due to a lack of understanding of the behaviour of the surfactants near the edges joining the various facets and in the ‘V-structures’, where the octapod ‘pods’ meet at the octahedral core. Instead, we base the effect of the steric hindrance on the following simple arguments. The ODPA has a surfactant molecule length of $H = 2.5 \text{ nm}$ ⁴⁵. Therefore, steric effects occur whenever any of the surfaces of the two octapods are within $2H = 5.0 \text{ nm}$ of each other. It is possible that this effect is diminished for a poor solvent³⁸, i.e., the range at which the steric repulsion dominates the vdW force occurs at closer separation than for a good solvent. Also, for a very sparse surfactant covering the steric effect should be reduced. To ensure a fair comparison of different configurations in all media, we define the maximum attractive vdW strength for a given u and v to be assumed at $1.5H$ separation in a good solvent. This value is precisely in the middle of the $H < r < 2H$ range. We chose this because the domination of the vdW force by steric repulsion is unlikely at $r = 2H$ but almost certain at $r = H$ based simple estimates using the theory in Ref. 38. Some interdigitation of the surfactants is probable before the steric effects start to dominate over the vdW interaction.

Hamaker-de-Boer results for the van-der-Waals interaction between two octapods. We compute the vdW interaction for 200 equidistant points in r with a separation of 0.30 nm starting from octapod-octapod contact ($r = 0$) for 7 conveniently chosen configurations, shown in Fig. S10 for toluene. The configurations in Fig. S10 (right) show the positions of the octapods at contact. The two right-most curves (i) and (ii) correspond to the vdW interaction energies in toluene, as discussed in the main text. Curve (iii) shows a configuration similar to the one in (ii). However, for the configuration in (ii) the pods are along each other as far as possible, whereas in (iii) we have positioned the pod in such a way that another octapod’s pod could symmetrically fit in the V-structure at a separation of $1.5H$. Configuration (iii) therefore has a similar U_{vdW} curve as the one for configuration (ii), which assumes lower values for the same separation r because the pods interact over a smaller area. The four left-most curves (vi,v,vi,vii) show the other configurations which we considered likely to occur in the experiments or were interesting to study. Note that curves (vi) and (vii) do not achieve the actual value of U_{vdW} near $r = 0$, because they do not diverge to $U_{\text{vdW}}(r \rightarrow 0) = -\infty$. This can be explained by the numerical difficulties that occur for such separations, especially for configurations where octapod contact occurs at a set of points. For configurations (iv) and (v) this is not as much of a problem, because of the larger contact area (at $r = 0$), namely line segments and a triangle, respectively. The interaction strength at $r = 2H$ is, however, not strongly influenced by this numerical problem at $r = 0$.

Proposed mechanism for hierarchical octapod self-assembly based on the simulations and theory. Using our Hamaker-de-Boer type calculations of the vdW interaction U_{vdW}

between two octapods, we indeed find that there is a strong attraction between the cores, configuration (i) in Fig. S10, of the octapods with a well depth of around $-3 kT$ at $r = 1.5H$ in toluene. We also found interactions of similar strength, configurations (ii) and (iii) in Fig. S11, which achieve $-2.5 kT$ and $-1.5 kT$ at $r = 1.5H$, between the pods of the octapods. However, these interactions decay faster with separation and are slightly less deep. In fact, for short distances U_{vdW} decays ranging from $U_{\text{vdW}} \propto r^{-14}$ to $U_{\text{vdW}} \propto r^{-18}$ are found for configurations (ii) and (iii). We therefore conjecture that in toluene configuration (i) in Fig. S10 is energetically more favourable, since (ii) and (iii) only become significant at much shorter separation, due to the faster decay. In addition, configurations (ii) and (iii) are probably more efficiently ‘passivated’, since the contact area of the octapods for these configurations is much greater. Therefore, we believe that the interlocking chain formation in toluene, shown in Fig 3a, is driven by this vdW core-core attraction. For chloroform the entire interaction potential is around 0.8 times the potential in toluene. This may be sufficient to prevent aggregation of octapods into larger structures for this solvent. We have verified that in the interlocking configuration (in toluene) there is sufficient interaction strength between the octapods to stabilize the chain. An octapod trapped in the cage formed by two adjacent octapods will experience vdW attractions between 2 and $6 kT$, depending on its exact position and the conformation of the cage. The curve that describes this combined effect is very similar to the one in Fig. S9b, only slightly wider and less deep. There is however insufficient direct support for stabilization of the chains using tip-tip interactions similar to the empiric model, nor can we exclude it on the basis of the results in Fig. S10. Not only are there too many unknowns for the behaviour of the steric repulsion due to the capping layer at the edges of the octapod, but the idealized model with its sharp edges and perfect crystal planes does not completely capture the conformation of the CdS at the tips of the octapods as observed by STEM tomography, see Fig. 1a. Even a small difference in the form or density of the capping layer can affect the U_{vdW} significantly. Another effect of this difference between the model and the actual octapod is that the minimum distance between two octapods in the interlocked chain for our model is slightly larger ($\approx 10\%$) than that observed in experiments. It is possible that for octapods coated with a capping layer tip-tip interactions are not necessary to fixate the interlocking chain configuration. Due to the capping layer the octapods becomes effectively thicker, which implies that the ‘cage’ formed by two adjacent octapods in a chain allows for a significantly reduced range of motion. In principle this could achieve the same effect as the short-ranged tip-tip interactions for the effectively thinner model without a capping layer. Proving this conjecture is however challenging and goes beyond the scope of the current investigation.

Based on the above observations for the strength of the ‘pod-pod’ vdW interactions, we hypothesize that the aggregation of chains into the 3D superstructures proceeds as follows with the addition of acetonitrile. The vdW interactions increase in strength, therefore the stabilization of existing interlocking chains is improved, which would explain the observation of stiffer chains. In addition, the interactions leading to aggregation of octapods into chains are also increased, thereby causing a lengthening of existing chains. This growth can occur either by single-octapod attachment or chain-chain attachment in an on-end manner. When the chains are of sufficient length, they will start to aggregate into larger clusters via side-by-side interactions. However, determining the number of octapods M necessary for side-by-side attachment to dominate over on-end attachment cannot be done as easily as for the simple LJ-SW model. However, in contrast with the empiric LJ-SW model, the tip-tip configuration

(Fig. S9d, the interaction energy of which was chosen to be large to achieve chain stabilization) for side-by-side attachment of two chains is no longer the energetically favoured one. Instead, it is the ‘pod-pod’ interaction, see Fig. 2 and configuration (iii) in Fig. S10, which for close proximity of the chains is similar in strength to the core-core attraction. At this point it is unclear whether there is an intermediate step between chain-chain aggregation and formation of the 3D superstructure, e.g., whether chains form sheets which then aggregate into the 3D superstructure.

Based on our simulations and theoretical work we have shown that the self-organization of the octapods is predominantly driven by the complex shape of the octapods through the anisotropic nature of the hard-particle and vdW interactions. The Hamaker-de-Boer type calculations indeed indicated that core-core interactions are indeed brought about by vdW forces. A natural step would be to improve upon the simple empiric LJ-SW model with the knowledge gained from the theoretical vdW analysis. However, we did not perform such additional simulations, because of the complexity of the vdW interaction and the difficulties in determining it. In addition the computational efficiency problems met in the LJ-SW empiric model simulations have thus far been prohibitive. We know that substantial changes to the depth and interaction range of the LJ potential, which would be required to give better correspondence to the theoretical result, will cause the chain-formation properties of the simple LJ-SW model to be lost at low densities. Furthermore, we believe that a simple model, which more accurately captures the calculated vdW interaction, thereby (hopefully) capturing the chain-formation and subsequent superstructure assembly, requires the use of several additional interaction sites or a far more complicated approximating potential function. We have already attempted to perform simulations with more interaction sites distributed over the pods of the octapod, but this led to prohibitively long simulation times for systems containing only a few octapods. It would definitely be worthwhile to revisit the simulations on the basis of the theoretical results, but we find this to go beyond the current possibilities of our numerical methods. Despite these caveats in our study of the hierarchical assembly of the octapods upon changing the environmental conditions, we are confident that the essential physics is captured by the proposed mechanism.

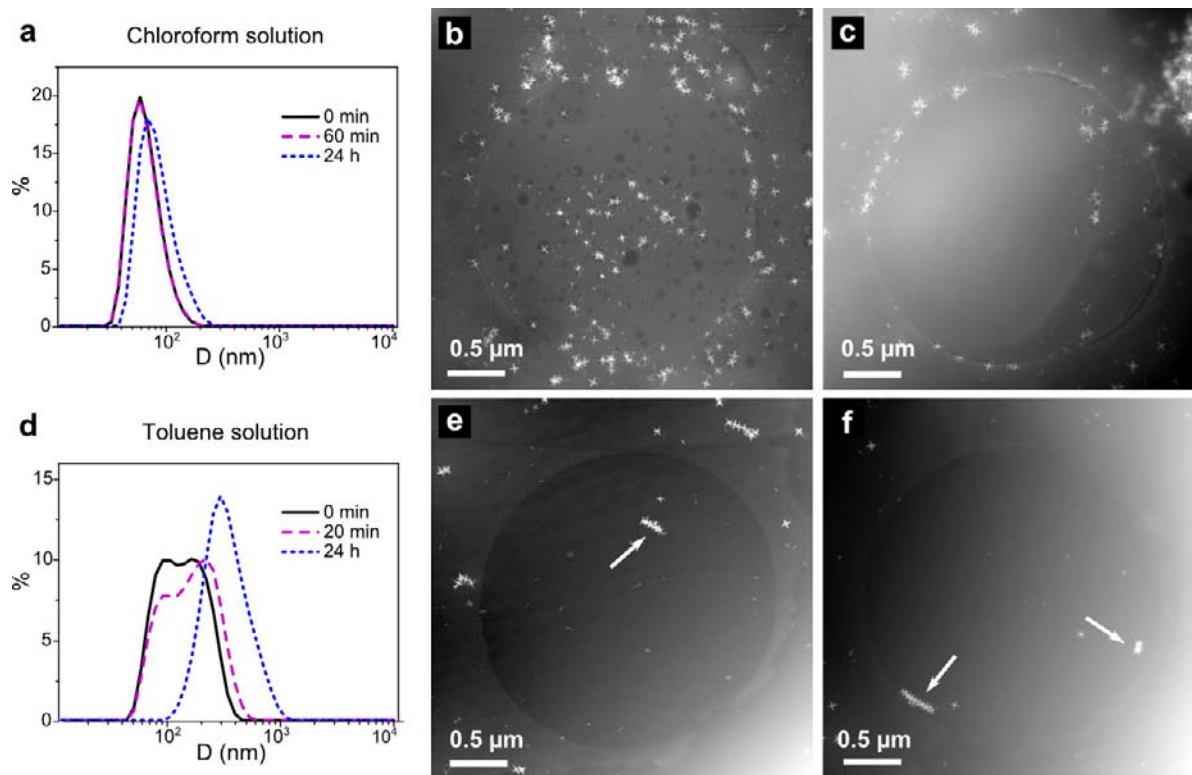
3. Supplementary Figures and Tables

Figure S1 | Comparison between octapods in chloroform solution and octapods in toluene solution. **a**, DLS cluster size distribution curves from octapods in chloroform solution, as a function of ageing time (D is the size of aggregates, % is the percentage frequency). **b,c**, Two representative STEM images from the frozen chloroform solution (~24 h ageing), showing no chains were formed. **d**, DLS cluster size distribution curves from octapods in toluene solution. **e,f**, Two representative STEM images from the frozen toluene solution (~24 h ageing). The white arrows mark chains in the solution.

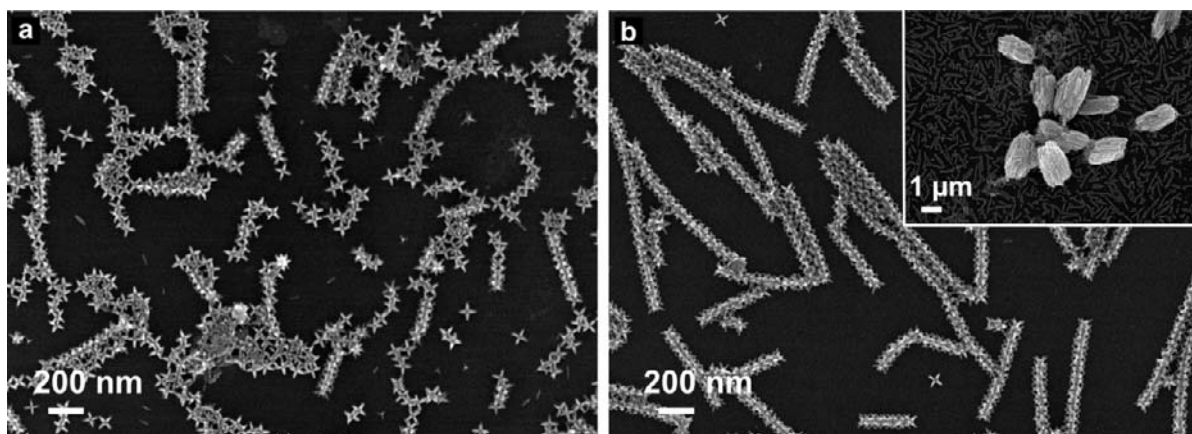


Figure S2 | Comparison between octapods in toluene solution and octapods in toluene/acetonitrile solution. **a**, SEM image from octapods in toluene solution after deposition on a silicon wafer. **b**, SEM image after addition of acetonitrile to the solution (see the discussion for details) used in **a** (the inset shows a lower magnification view in which 3D clusters are visible). Single chains or groups of chains are visible in the wetting layer between the clusters, with clearly longer chains than in toluene.

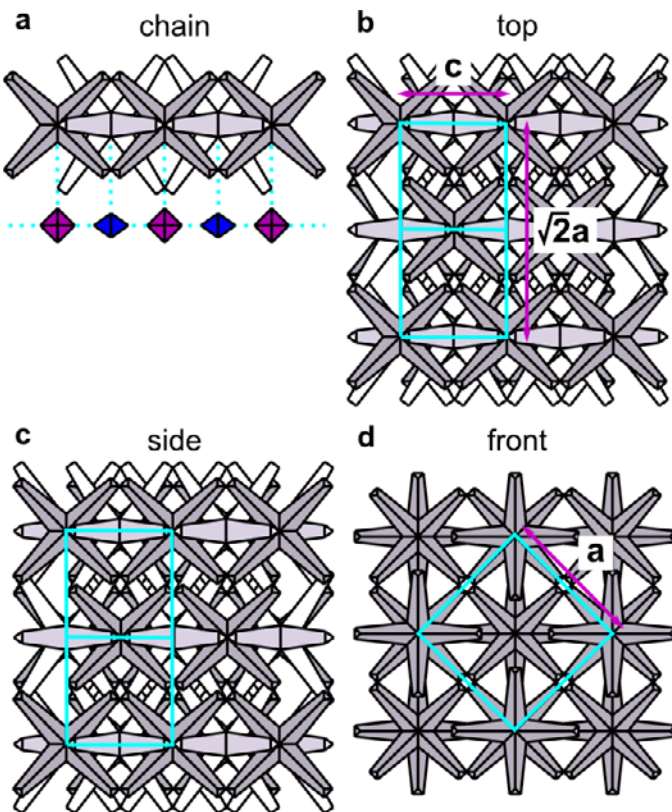


Figure S3 | Sketches of superstructures. **a**, Sketch of the octapods ‘interlock’ in a chain. The octapods can have two orientations (magenta octahedron and blue octahedron), each rotated with respect to the other by 45° along the chain axis (and corresponding to the $\langle 100 \rangle$

direction of the cube spanned by the tips of an octapod). **b-d**, Different views of the 3D superstructure formed by chains aggregation. Note that the top and side views are the same, as expected for a tetragonal unit cell (depicted by cyan lines). The orientation of the structure in the figure is chosen to be the same as the one found relative to the substrate we deposited the solution on for SEM imaging.

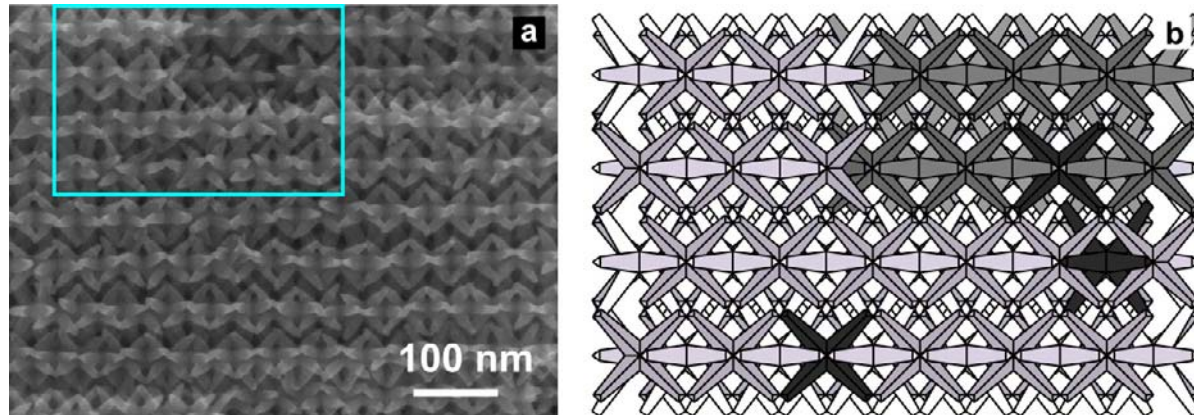


Figure S4 | Close view of the 3D superstructure. **a**, SEM image of a portion of a cluster deposited on silicon. The cyan box marks a region in which interruption of two chains is seen, revealing the octapod layer underneath, along with other defects. **b**, The proposed structure of the marked region in the SEM image, from which the tetragonal symmetry can be discerned. The dark grey octapods belong to the lower layer. Black octapods mark the missing octapods in the corresponding region of the SEM image.

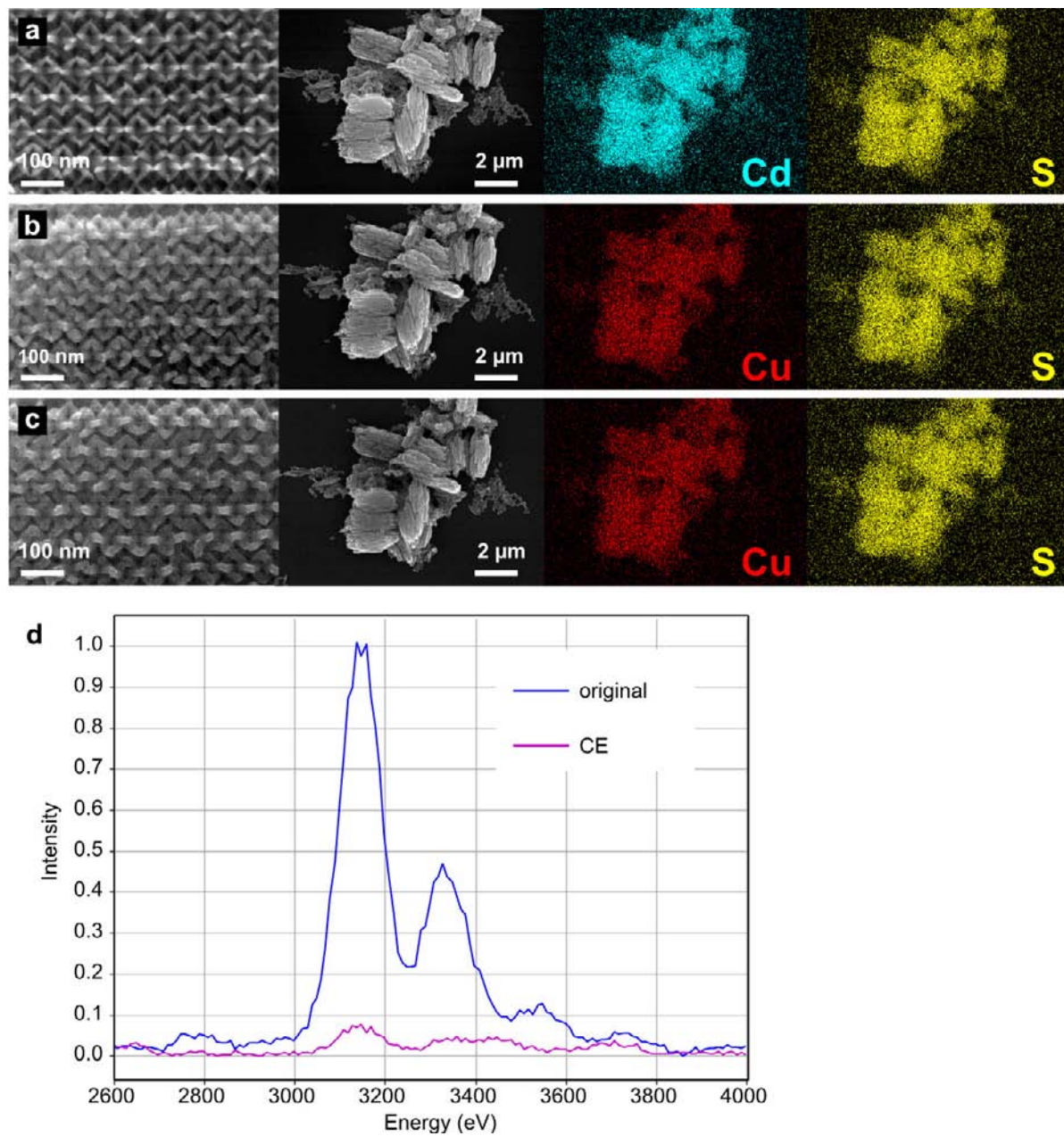


Figure S5 | SEM and EDS chemical maps after cation exchange (CE) and O₂ plasma treatment (CEP). **a**, SEM close-up view, SEM low magnification, Cd chemical map, and S chemical map from assemblies as synthesized. **b**, SEM close-up view, SEM low magnification, Cu chemical map, and S chemical map from assemblies after Cd²⁺ to Cu⁺ ion exchange (CE). **c**, Same as **b** after additional O₂ plasma treatment (CEP). **d**, Comparison between Cd L peaks from EDS on a large region before Cd²⁺ to Cu⁺ ion exchange (original), and after ion exchange (CE).

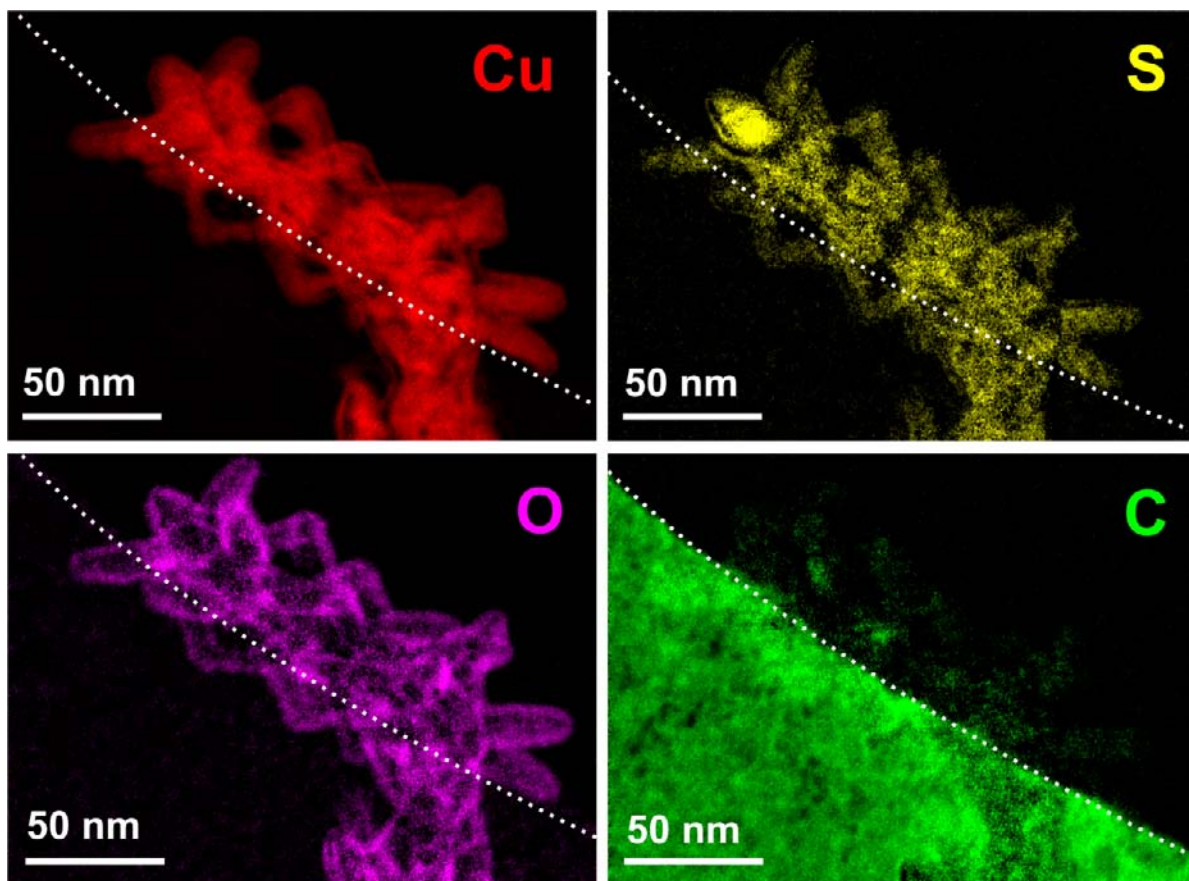


Figure S6 | EFTEM chemical maps from a chain after cation exchange and O₂ plasma treatment (CEP). Elemental maps obtained in energy filtered TEM (EFTEM) from copper L edge (red) at 931 eV, sulphur L edge (yellow) at 165 eV, oxygen K edge at 532 eV (magenta), and carbon K edge at 284 eV (green) obtained from the same chain portion after deposition on a holey carbon grid, followed by the same treatment of sample (CEP) of Fig. S5c. The dotted lines mark the edge of the carbon support film of the TEM grid.

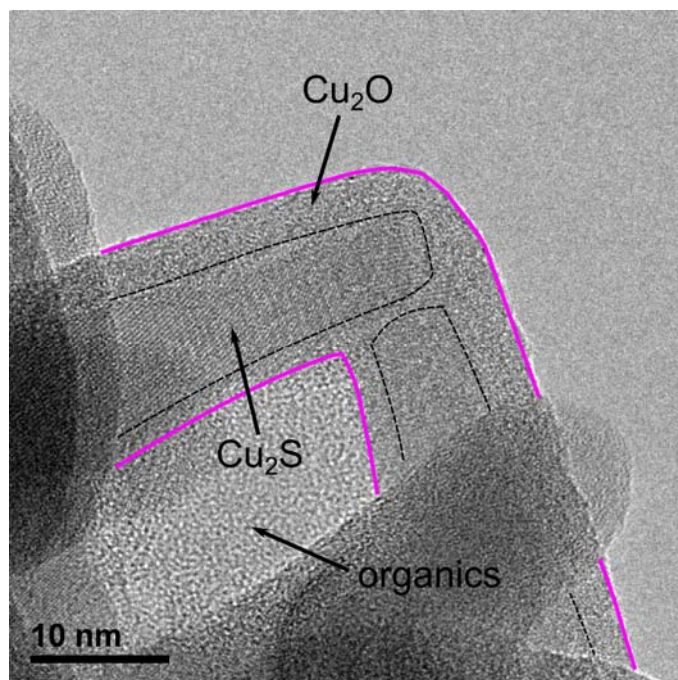


Figure S7 | HRTEM image of a chain detail after cation exchange and O_2 plasma treatment (CEP). The region shows a detail of two welded tips after plasma treatment. The oxide layer (~3 nm thick) is mainly amorphous. A brighter (i.e., lighter) amorphous structure is also visible in an interstitial region, probably coming from residual organic species.

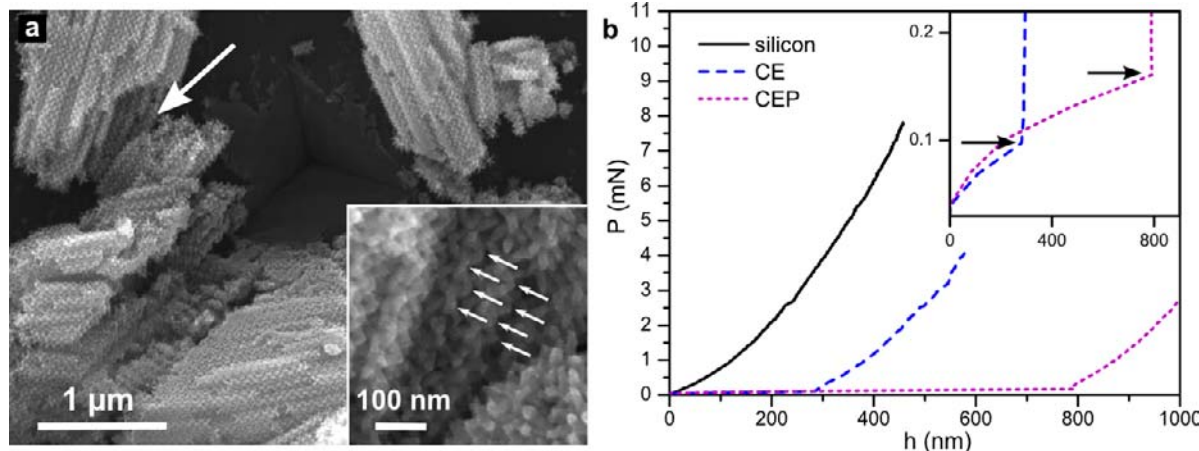


Figure S8 | Typical indentation imprint and load-depth (P - h) curves. **a**, Indentation imprint on a group of 3D structures after cation exchange followed by O_2 plasma treatment (CEP). Although the centre of the imprint is on the silicon substrate, therefore making the measurement not significant, the tip did fracture the structure on the top left corner, displacing part of it and revealing the inner layers. On the high-magnification inset of that area, welded octapod pods can be seen (indicated by arrows), confirming the penetration of the plasma oxidation into the inner layers. **b**, In black, the typical loading curve on silicon. In

blue and magenta, before reaching the substrate, the tip cuts through 3D structures that underwent cation exchange (CE), and both cation exchange and O₂ plasma treatments (CEP), respectively. The load reached (indicated in the inset by the arrow) is an indirect measurement of the toughness of the structure, which in average was found to be higher for the CEP structures (h is the penetration depth and P is the tip force).

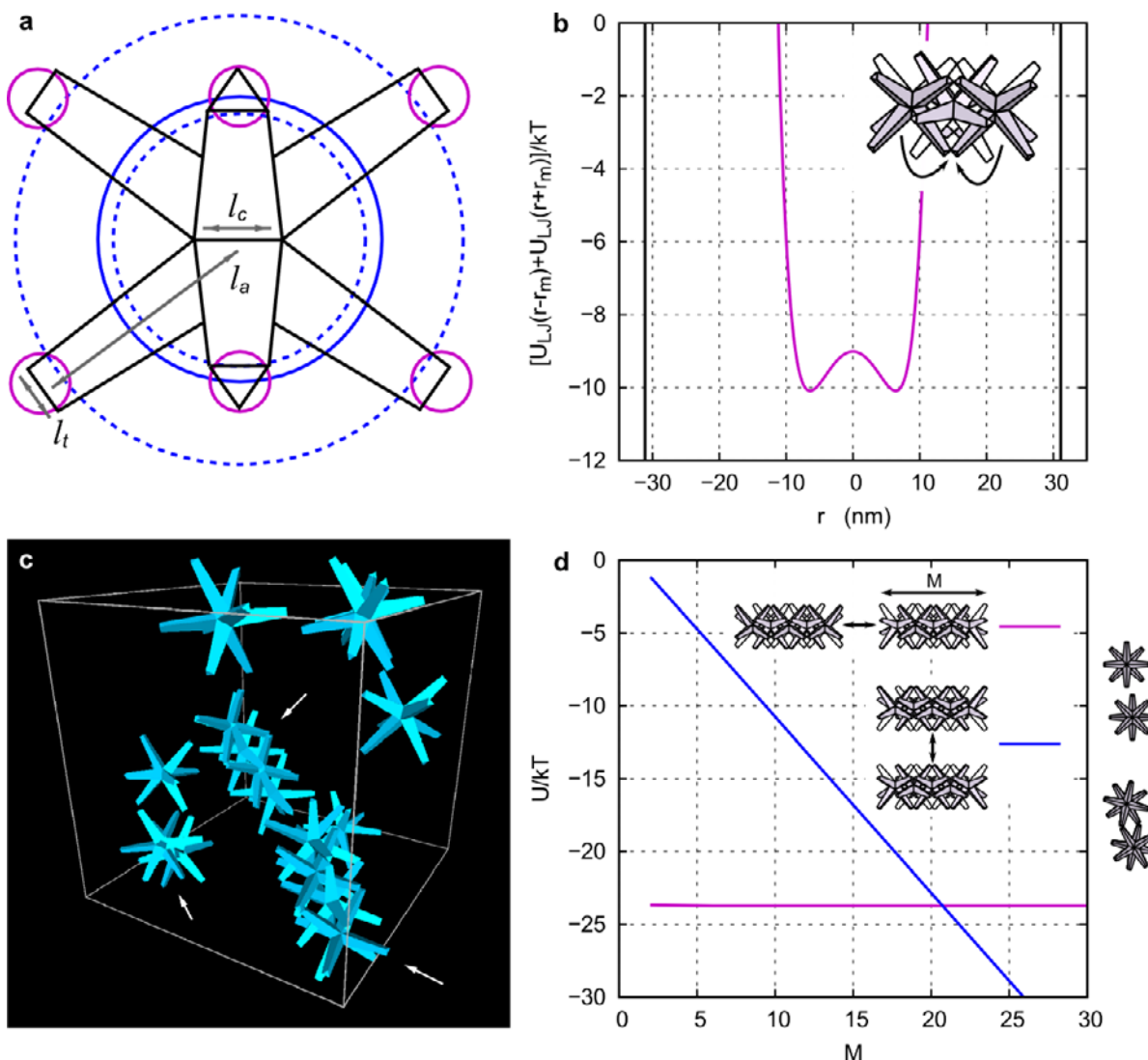


Figure S9 | Empiric model for chain formation of octapods in simulation studies. **a**, The two-dimensional (2D) projection of the three-dimensional (3D) octapod model for the octapods used in our simulations. The core edge length is given by $l_c = 22$ nm, the tip edge length by $l_t = 15$ nm, and the pod length by $l_a = 62$ nm. The various 3D potential wells used have also been drawn. The magenta circles indicate the range of the tip-tip square-well (SW) interaction ($U_{SW}(r) \approx -4$ kT), the blue circles indicate the Lennard-Jones interaction (LJ). The dashed blue circles indicate for which r the value of $U_{LJ}(r)$ equals -1 kT, and the solid blue circle indicates r_m for which $U_{LJ}(r)$ assumes its minimum ($U_{LJ}(r) \approx -8$ kT). Note that the magenta circles appear to be off centre for the ‘pods’ in the plane of the paper. This is caused

by projection. **b**, The interaction strength (in kT) experienced by an octapod in the cage formed by two adjacent octapods in the interlocking configuration (indicated by the black arrows), as a function of the deviation from the centre of the cage, which we locate at $r = 0$. The two vertical black lines indicate for which r the octapod comes into contact with the adjacent octapods. Note the slight double-well nature of the combined interaction potential, which is not significant for the chain formation. **c**, A snapshot of an *NVT* MC simulation in a cubic box, containing 16 of the empiric octapod models at a volume fraction of $\phi \approx 0.01$. Several of the octapods have formed interlocked chains, indicated with white arrows. Two segments of length four and one dimer can be observed. **d**, The theoretically established aggregation energy U (at contact) in kT as a function of the number of octapods in an interlocked chain M for two possible configurations. The magenta curve gives the energy associated with on-end attachment of two chains of length M , which is nearly constant with M . The blue curve gives the energy associated with side-by-side aggregation of chains of equal length, for the energetically most favoured configuration. The two energies become comparable for $M = 20$ octapods in a chain. Note that a double tip-tip configuration is favoured for side-by-side aggregation; the transition to this configuration is shown to the right of the graph.

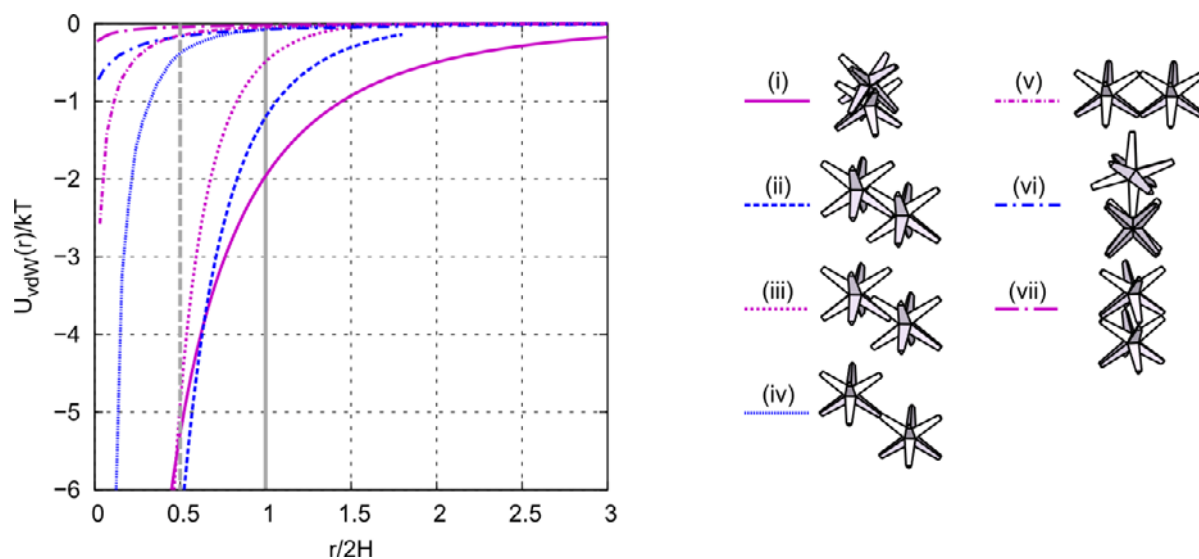


Figure S10 | The van-der-Waals (vdW) interaction strength between two octapods in toluene for several configurations. We have determined the non-retarded vdW interaction strength U_{vdW} in terms of the thermal energy kT , with k Boltzmann's constant and T the temperature, as a function of the distance r between the octapods' cores for 7 configurations, which are schematically given on the right and have been labelled with Roman numerals. The distance r has been expressed in terms of $2H$, where $H = 2.5$ nm is the length of a fully extended octadecylphosphonic acid (ODPA) molecule, which covers the surface of the octapod. The dashed grey line indicates $r = H$. Somewhere in the region $H < r < 2H$ the steric repulsion effected by the presence of the capping layer is believed to dominate over the vdW interaction. Note that configurations (ii) and (iii) differ only slightly. For configuration (ii) 'pod-pod' surface contact is optimized, whereas for configuration (iii) the position of the pod

is such that another pod (of a third octapod) can be placed symmetrically into the V-structure formed by the ‘pods’ of the second octapod. As explained in the text, configurations (vi) and (vii) suffer from numerical convergence problems near $r = 0$, i.e., U_{vdW} does not diverge to $-\infty$.

4. Supplementary Notes

References

34. Fultz B. & Howe J.M. *Transmission electron microscopy and diffractometry of materials* Ch.4 (Springer-Verlag, Berlin Heidelberg, 2008).
35. Filion, L. *et al.* Efficient method for predicting crystal structures at finite temperature: variable box shape simulations. *Phys. Rev. Lett.* **103**, 188302 (2009).
36. de Graaf, J., Dijkstra, M. & van Roij, R. Triangular tessellation scheme for the adsorption free energy at the liquid-liquid interface: towards non convex patterned colloids. *Phys. Rev. E* **80**, 051405 (2009).
37. GAMMA Research Group at the University of North Carolina. RAPID - Robust and Accurate Polygon Interference Detection. <http://gamma.cs.unc.edu/OBB/> (1997).
38. Israelachvili, J. N. *Intermolecular and Surface Forces* Ch.11 (Academic Press, London, 1991).
39. Striolo, A. *et al.* Molecular weight, osmotic second virial coefficient, and extinction coefficient of colloidal CdSe nanocrystals. *J. Phys. Chem. B* **106**, 5500–5505 (2002).
40. Bergström, L. Hamaker constants of inorganic materials. *Adv. Colloid Interface Sci.* **70**, 125–169 (1997).
41. Cao, G. *Nanostructures & Nanomaterials: Synthesis, Properties & Applications* Ch.2 (Imperial College Press, London, 2004).
42. Butt, H.-J., Graf, K. & Kappl, M. *Physics and Chemistry of Interfaces* Ch.6 (Wiley-VCH, Weinheim, 2003).
43. Takenaga, M., Jo, S., Graupe, M. & Lee, T. R. Effective van der Waals surface energy of self-assembled monolayer films having systematically varying degrees of molecular fluorination. *J. Colloid Interface Sci.* **320**, 264–267 (2008).
44. Anand, M. *et al.* Thermodynamic analysis of nanoparticle size selective fractionation using gas-expanded liquids. *Ind. Eng. Chem. Res.* **47**, 553–559 (2008).
45. Woodward, J. T., Ulman, A. & Schwartz, D. K. Self-assembled monolayer growth of octadecylphosphonic acid on mica. *Langmuir* **12**, 3626–3629 (1996).